applied sciences

MDPI

Article

Intelligent Demodulation of Overlapping Spectra in FBG-PMFBG Sensing Based on a Spiking Neural Network

Bawoke Simachew [1], Cheng-Kai Yao [2], Wei-Lun Wu [2], Ya-Lin Chen [2], Cheng-Zuo Tsai [2], Pei-Chung Liu [2], Yibeltal Chanie Manie [2], Amare Mulatie Dehnaw [3], Yang-Lang Chang [1] and Peng-Chun Peng [2,*]

[1] Department of Electrical Engineering, National Taipei University of Technology, Taipei 10608, Taiwan; t109319401@ntut.org.tw (B.S.); ylchang@ntut.edu.tw (Y.-L.C.)
[2] Department of Electro-Optical Engineering, National Taipei University of Technology, Taipei 10608, Taiwan; t111659004@ntut.org.tw (C.-K.Y.); t113658034@ntut.edu.tw (W.-L.W.); t113658068@ntut.edu.tw (Y.-L.C.); t114658007@ntut.org.tw (C.-Z.T.); t113658043@ntut.edu.tw (P.-C.L.); yibeltal_chanie@ntut.edu.tw (Y.C.M.)
[3] Department of Vehicle Engineering, National Taipei University of Technology, Taipei 10608, Taiwan; amare.mulatie@ntut.edu.tw
* Correspondence: pcpeng@ntut.edu.tw; Tel.: +886-2-2771-2171 (ext. 4671)

Abstract

This paper presents a leaky integrate-and-fire spiking neural network (LIF-SNN) for direct demodulation of spectrally overlapped fiber Bragg grating–polarization-maintaining fiber Bragg grating (FBG–PMFBG) responses. The hybrid spectrum contains one conventional FBG peak and two PMFBG peaks, producing partial-to-severe overlap as the FBG wavelength shifts toward either PMFBG peak. Because controlled overlap measurements are costly, data acquisition is concentrated in informative overlap regions. The proposed LIF-SNN uses surrogate-gradient learning and temporal spike integration to directly estimate all three peak wavelengths without explicit peak separation. Multi-seed validation, additive white Gaussian noise (AWGN) augmentation, and few-shot fine-tuning further improve robustness under limited measured data. On the held-out test set, the model achieves a mean absolute error (MAE) of 0.0786 nm and a mean squared error (MSE) of 0.0130 nm^2, outperforming mixture density network (MDN), long short-term memory (LSTM), and gated recurrent unit (GRU) baselines. Few-shot adaptation reduces the MSE to 0.0085 nm^2, while 30–50 dB signal-to-noise ratio (SNR) tests show consistently lower MAE than the compared models. A matched non-spiking multilayer perceptron (MLP) ablation further shows that performance depends on both architecture and training strategy: the MLP remains competitive on clean experimental spectra, whereas the LIF-SNN shows stronger robustness under noise and benefits from AWGN augmentation and adaptation. These results demonstrate accurate, adaptive, and noise-robust three-peak demodulation for overlap-affected FBG–PMFBG strain sensing.

Keywords: fiber Bragg grating (FBG); polarization-maintaining fiber Bragg grating (PMFBG); spiking neural network (SNN); spectral overlap; wavelength demodulation; strain sensing; noise robustness; few-shot adaptation

Check for updates

Academic Editor: Petros Nicopolitidis

Received: 19 September 2026
Revised: 8 October 2026
Accepted: 14 October 2026
Published: 16 October 2026

Copyright: © 2026 by the authors. Licensee MDPI, Basel, Switzerland. This article is an open access article distributed under the terms and conditions of the Creative Commons Attribution (CC BY) license.

1. Introduction

Optical fiber sensors (OFSs) have become important sensing technologies because of their high sensitivity, compact size, immunity to electromagnetic interference, and strong multiplexing capability, making them suitable for applications in aerospace, energy, and structural health monitoring (SHM) [1–5]. Among them, FBG sensors are particularly

attractive because they enable wavelength-encoded sensing through shifts in the reflected Bragg wavelength induced by external perturbations such as strain and temperature [6–10]. To increase sensing capacity, multiple FBGs can be integrated along a single fiber using intensity–wavelength-division multiplexing techniques [11]. However, strain-induced wavelength shifts can reduce the spectral separation between neighboring responses and may lead to partial or severe peak overlap, thereby degrading peak identification and wavelength-demodulation accuracy [11].

Recently, machine learning and deep learning (DL) methods have been introduced for spectral reconstruction, overlap resolution, and wavelength estimation [12–17]. These approaches improve nonlinear modeling capability but may remain sensitive to training-data availability, initialization, measurement noise, and changes in overlap severity. In fiber-optic sensing applications, obtaining large quantities of experimentally measured spectra is costly and time-consuming [17]; consequently, learning-based demodulation methods increasingly employ data augmentation, transfer learning, meta-learning, or deep feature extractors to improve generalization [17]. Nevertheless, robust wavelength recovery remains difficult when individual peaks are no longer visually separable, and the informative spectral features are distributed across a congested wavelength region. Recent developments in spiking neural networks provide an alternative to conventional continuous-valued neural processing by representing information through discrete spike events and membrane dynamics. Such temporal and event-driven processing has attracted increasing interest in efficient and adaptive sensing, particularly in neuromorphic and resource-constrained systems [18–20]. Related studies further indicate that the organization of spiking activity and membrane dynamics can influence information representation, robustness, and computational efficiency [18,20]. These characteristics motivate investigating SNNs for spectral demodulation, where wavelength information must be recovered from globally distributed and partially obscured spectral features rather than from isolated local maxima.

Overlapped FBG–PMFBG sensing further increases the demodulation challenge because a conventional FBG contributes one dominant reflection peak, whereas a PMFBG produces two peaks corresponding to its fast and slow axes [21–23]. As the strain-sensitive FBG wavelength shifts toward either PMFBG peak, the resulting three-peak spectrum can evolve from separated responses to partial or severe superposition, making local-maximum detection and unconstrained peak fitting increasingly ambiguous. Reliable operation under such spectral congestion therefore requires estimation of the underlying peak centers from the complete measured spectrum. Hybrid PMFBG–FBG architectures have been demonstrated for multi-parameter sensing [23]; however, to the best of our knowledge, direct demodulation of spectral overlap between a conventional FBG and the two polarization-resolved peaks of a PMFBG remains largely unexplored. This work addresses this gap using a LIF-SNN that directly estimates the three underlying peak wavelengths from the composite spectrum without explicit peak separation. Because extensive acquisition of experimentally controlled overlap spectra is costly and time-consuming, measurements are intentionally concentrated in the most informative partial-to-severe overlap regions, including approximately four to six representative cases covering different peak-interaction positions and overlap severities.

The proposed framework combines surrogate-gradient learning and temporal spike integration with validation-selected AWGN augmentation and few-shot fine-tuning. AWGN augmentation is selected using multi-seed clean-validation MSE, robustness is evaluated under controlled SNR degradation, and adaptation is assessed using disjoint support and query sets. These strategies are designed to improve generalization and adaptation under limited measured data while preserving accurate estimation of the strain-sensitive FBG

peak and the PMFBG fast- and slow-axis peaks. Existing learning-based FBG demodulation studies have addressed wavelength estimation and spectral overlap using conventional neural architectures, whereas direct three-peak demodulation of hybrid FBG–PMFBG spectra using an SNN remains insufficiently explored. Accordingly, this study investigates whether the proposed LIF-SNN can accurately recover the three FBG–PMFBG peak wavelengths under partial-to-severe spectral overlap, whether the observed performance differences are associated with the spiking architecture itself or with the use of AWGN augmentation and few-shot adaptation, and how stable the demodulation remains across repeated training runs, peak-specific conditions, and controlled noise degradation.

The main contributions are summarized as follows:

1. FBG–PMFBG overlap demodulation: A LIF-SNN framework is developed for wavelength estimation under partial and severe overlap between the FBG peak and the PMFBG peaks.
2. Direct three-peak localization: The rate-coded SNN simultaneously estimates the FBG and PMFBG fast- and slow-axis peak centers directly from congested composite spectra without explicit peak separation.
3. Limited-data robustness and adaptation: Multi-seed AWGN augmentation selection and few-shot fine-tuning are incorporated to improve generalization under noise-degraded and data-limited conditions.
4. Experimental validation: Performance is evaluated on measured spectra against MDN, LSTM, and GRU baselines using wavelength-error metrics, error-distribution analysis, few-shot adaptation, and SNR-dependent robustness testing.

2. Experimental Configuration of the Proposed FBG–PMFBG Sensing System

Figure 1 illustrates the experimental configuration and signal-processing pipeline of the proposed hybrid FBG–PMFBG sensing system. The setup consists of a broadband light source (BLS), an optical circulator, a one-by-two optical coupler (C), a PMFBG, an FBG, and an optical spectrum analyzer (OSA). Light from the BLS is launched into Port 1 of the circulator and routed from Port 2 to the optical coupler, where it is divided into two sensing branches. The PMFBG and FBG are connected to separate branches of the coupler. The FBG is mounted on a clamping fixture integrated with a translation stage for controlled strain loading, whereas the PMFBG remains unstrained. The PMFBG has a grating length of 10 mm, an FWHM of 0.25 ± 0.05 nm, and reflectivity greater than 80%. Its measured fast- and slow-axis reflections are located at approximately 1545 ± 0.05 nm and 1546 ± 0.05 nm.

In this hybrid configuration, the strain-dependent FBG reflection and the PMFBG reflections form a three-peak spectral response within the same wavelength window. As strain is applied to the FBG, its Bragg wavelength shifts toward and may overlap with either PMFBG peak, causing the measured spectrum to evolve from well-separated responses to partial overlap and severe multi-peak superposition. This controlled spectral evolution provides the experimental basis for evaluating three-peak wavelength demodulation under different overlap conditions. The mechanically fixed PMFBG is used here to generate controlled and identifiable overlap conditions; it is an experimental simplification rather than a requirement of the demodulation principle.

In the intended sensing architecture, the acquired optical response is transmitted to the central office (CO) for processing, while the present laboratory implementation emulates this stage locally. The reflected spectra are redirected by the circulator to the OSA and acquired over 1540–1550 nm with a nominal resolution of 0.03 nm (actual: 0.031 nm). Each spectrum contains 1001 points with a 0.010 nm sampling interval, with no additional point

averaging or spectral smoothing. The measured spectra are then processed by the proposed SNN to estimate the FBG and PMFBG fast- and slow-axis peak wavelengths.

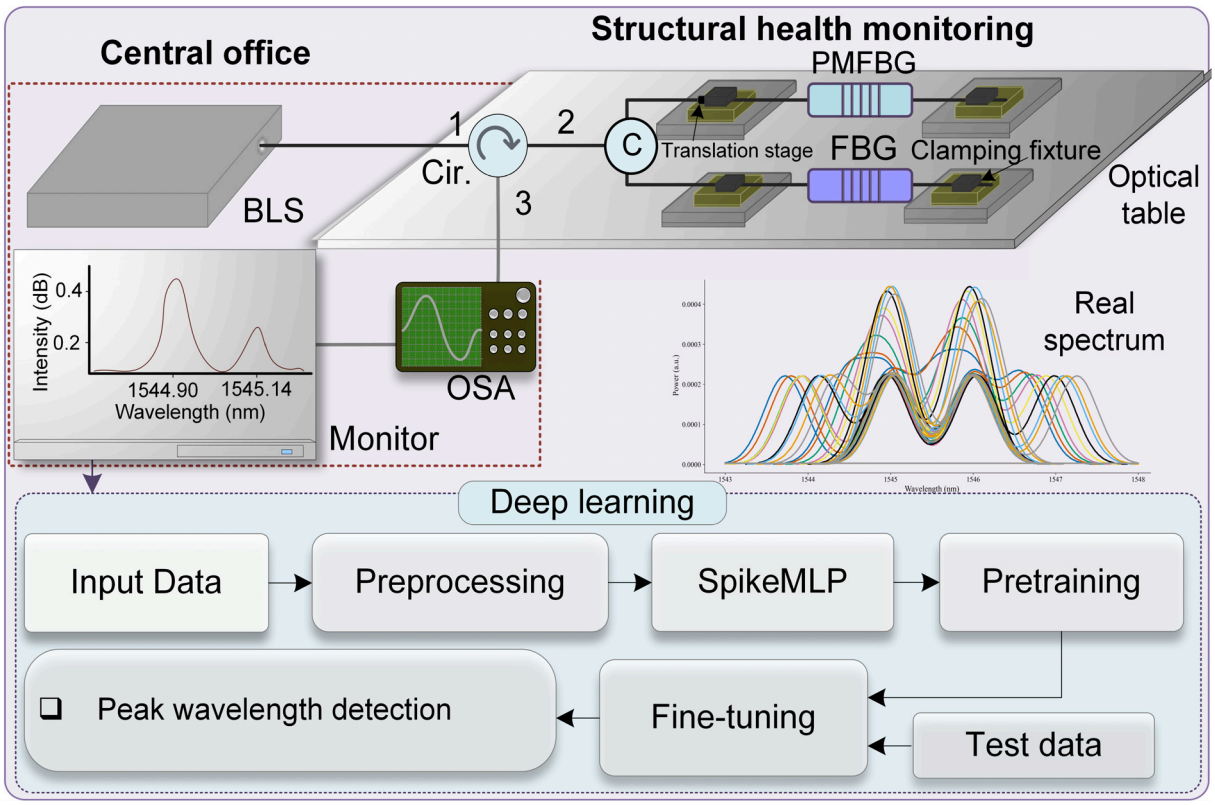


Figure 1. Experimental setup and signal-processing pipeline of the proposed hybrid FBG–PMFBG sensing system.

3. FBG–PMFBG Demodulation Under Spectral Overlap Conditions

3.1. Physics-Based Peak Modeling and Overlap Definition

FBG demodulation is commonly based on estimation of the Bragg wavelength from the measured reflection spectrum. For an isolated reflection, the spectral profile can be approximated by a Gaussian function, providing a physically interpretable representation of the peak center, amplitude, and linewidth [11]. Such parametric representations are effective when individual reflections are sufficiently separated; however, direct peak search or independent curve fitting becomes increasingly ambiguous when neighboring spectral components overlap or exhibit unequal amplitudes, as modeled in (1).

$$I(\lambda;\lambda_B, I_p, \Delta\lambda_{FWHM}) = I_p exp\left[-4ln(2)\left(\frac{\lambda-\lambda_B}{\Delta\lambda_{FWHM}}\right)^2\right] \quad (1)$$

where λ_B denotes the Bragg (central) wavelength, I_p represents the peak reflectivity amplitude, and $\Delta\lambda_{FWHM}$ is the full width at half maximum (FWHM), which defines the spectral linewidth at half of the peak intensity.

In the hybrid configuration, the measured spectrum contains the strain-dependent FBG reflection together with the fast- and slow-axis PMFBG reflections. Spectral overlap is characterized according to the center-to-center separation of adjacent peaks relative to their spectral linewidths. For adjacent components with center wavelengths λ_i and λ_j, the wavelength separation is defined in (2):

$$\Delta\lambda_{ij} = |\lambda_i - \lambda_j| \quad (2)$$

In this study, overlap severity is characterized by the center-to-center wavelength separation, $\Delta\lambda_{ij}$, between neighboring peaks together with their spectral widths, quantified by the FWHM. Because peak resolvability depends not only on center-to-center separation but also on FWHM and amplitude, no single fixed separation threshold is used.

3.2. Hybrid Spectral Congestion in FBG–PMFBG Sensing

The hybrid FBG–PMFBG configuration produces a three-component spectral response consisting of one FBG reflection and the fast- and slow-axis reflections of the PMFBG. The PMFBG fast- and slow-axis responses provide two distinct spectral references, while the FBG peak shifts with applied strain. Consequently, the relative spacing between the FBG reflection and either PMFBG component decreases as the FBG wavelength approaches the corresponding polarization peak. The measured dataset includes severe-overlap cases in which the moving FBG peak approaches either PMFBG peak until their center wavelengths become nearly coincident.

When the peak spacing becomes comparable with the component linewidths, the individual responses merge into a composite spectral profile. Under partial overlap, individual spectral features may remain distinguishable, whereas under severe overlap the local maxima and valleys can become strongly distorted. In such cases, conventional peak detection may no longer provide an unambiguous estimate of the underlying centers.

The present experiment therefore focuses specifically on wavelength demodulation under controlled hybrid spectral congestion. Broader multi-parameter or large-scale network operation is not assumed as an experimentally demonstrated capability; rather, the hybrid configuration provides a representative three-peak sensing problem in which the strain-dependent FBG response interacts with two approximately stationary PMFBG reference peaks.

3.3. SNN-Based Demodulation of Overlapped Spectra

The proposed SNN receives the normalized measured spectrum x and directly estimates the three peak centers corresponding to the FBG, PMFBG fast-axis, and PMFBG slow-axis responses. The static input spectrum is repeatedly presented over T temporal steps, allowing the spiking neurons to integrate spectral information through their membrane dynamics [18,24]. The resulting temporal spike activity forms an event-driven representation of the spectral response. The output spike trains are then converted into a continuous rate-coded representation, which is passed through the regression head to estimate the three-element wavelength vector. Unlike continuous-valued artificial neural network (ANN) activations, the SNN distributes the spectral representation across membrane states and discrete spike events over the temporal window, providing a temporally integrated representation of the composite spectrum [18–20,25].

3.3.1. LIF Dynamics and Spike Generation

The neurons in the proposed SNN follow LIF dynamics [24,26]. For neuron j at time step t, the membrane potential is updated according to (3).

$$V_{j,t} = \beta V_{j,t-1} + I_{j,t} \tag{3}$$

where β is the membrane decay factor (typically $0 < \beta < 1$), $V_{j,t-1}$ is the previous membrane potential of neuron j at time step t, and $I_{j,t}$ denotes the input current to neuron j at time step t, obtained from the encoded spectral features. This leaky integration mechanism enables the neuron to accumulate information across temporal steps, while the membrane decay factor controls the temporal retention of the membrane potential.

A spike is generated when the membrane potential exceeds the firing threshold, as given (4) [24,26]:

$$S_{j,t} = \begin{cases} 1, & \text{if } V_{j,t} \geq V_{th} \\ 0, & \text{otherwise} \end{cases} \tag{4}$$

where Vth is the firing threshold. After spike generation, the membrane potential is reset using the multiplicative reset rule in (5).

$$V_{j,t} \leftarrow V_{j,t}(1 - S_{j,t}) \tag{5}$$

This temporal integration provides an alternative representation of the congested spectral response and is evaluated experimentally in this work for its contribution to overlap demodulation and noise robustness.

3.3.2. Surrogate Gradient for Backpropagation

The spike-generation function in (4) is non-differentiable; therefore, direct backpropagation is not applicable. To enable gradient-based optimization, a surrogate gradient is adopted during the backward pass [18,26], as defined in (6):

$$\frac{\partial S}{\partial V} \approx g(v) = \frac{1}{1 + |v|}, \; v = V_{j,t} - V_{th} \tag{6}$$

This approximation makes it possible to train the SNN end-to-end using gradient-based optimizers while preserving discrete spike generation in the forward pass. In this work, the surrogate-gradient framework allows efficient optimization using modern training strategies within standard DL environments [24].

3.3.3. Rate Decoding and Peak-Center Regression

Let $S_t^{(L)}$ denote the output spikes of the final spiking layer at time step t. The temporal spike train is converted into a continuous representation through rate coding [26]:

$$Rate^{(L)} = \frac{1}{T}\sum_{t=1}^{T} S_t^{(L)} \tag{7}$$

where T is the number of temporal steps. The rate-coded representation is then passed to a fully connected regression layer to estimate the peak centers, as expressed in (8):

$$\hat{y} = FC_{out}(Rate^{(L)}) \tag{8}$$

where $\hat{y} = \left[\hat{\lambda}_B, \hat{\lambda}_f, \hat{\lambda}_s\right]^T$ contains the estimated FBG, PMFBG fast-axis, and PMFBG slow-axis peak centers.

This formulation allows the network to transform temporally accumulated spiking activity into precise wavelength predictions.

3.3.4. Training Objective and Adaptation Protocol

The proposed SNN is trained using the MSE between the predicted and reference peak-center vectors, where the squared errors are averaged over the three wavelength outputs and all spectra in each mini-batch, as defined in (9) [10,11].

$$L_{MSE} = \frac{1}{3M}\sum_{m=1}^{M} \|y_m - \hat{y}_m\|_2^2 \tag{9}$$

where M is the batch size, y_m denotes the ground-truth peak-center vector, and $\hat{y}_m$ denotes the corresponding SNN prediction.

Training and adaptation are treated as two distinct stages. During pretraining, the SNN learns the mapping between the measured composite spectra and their associated three-peak wavelength vectors. AWGN augmentation is applied only to training-parent spectra, with the augmentation ratio selected using multi-seed performance on the clean validation set. Few-shot adaptation is subsequently performed using a separate support set, and the operational number of gradient updates is selected from the predefined 0–12-step budget using validation performance. This separation distinguishes operational fine-tuning from long-horizon adaptation analysis.

4. Data Acquisition and SNN Implementation

4.1. Dataset and Preprocessing

The conventional FBG exhibits an initial Bragg wavelength near 1544 nm, while the PMFBG produces two reflection peaks near 1545 and 1546 nm. Measurements are acquired under laboratory conditions at approximately 23 °C. Temperature is not treated as an independent sensing variable in this study; therefore, any residual room-temperature variation is regarded as part of the existing experimental background rather than a controlled input to the demodulation model. Strain is applied only to the conventional FBG, while the PMFBG remains unstrained. As the applied strain increases, the FBG Bragg wavelength shifts relative to the two PMFBG peaks, causing the measured spectra to evolve from well-separated responses to partial overlap and severe spectral superposition.

The experimental dataset comprises 46 measured spectra, partitioned into 36 training spectra, 5 validation spectra, and 5 held-out test spectra, corresponding approximately to an 80%/10%/10% split. The validation and test subsets remain strictly excluded from model training and augmentation. All spectra are mapped to a common wavelength grid and normalized using the mean and standard deviation computed from the training subset only. These training-derived normalization parameters are then applied unchanged to the validation and test subsets to prevent information leakage.

For each spectrum, the target output is a three-element wavelength vector representing the FBG Bragg wavelength and the PMFBG fast- and slow-axis peak centers. The SNN learns a direct mapping from the normalized composite spectrum to these three wavelengths without handcrafted features or explicit peak separation. Figure 2 shows the strain distributions of the training, validation, and held-out test subsets, which span the investigated strain range and the corresponding spectral-overlap conditions.

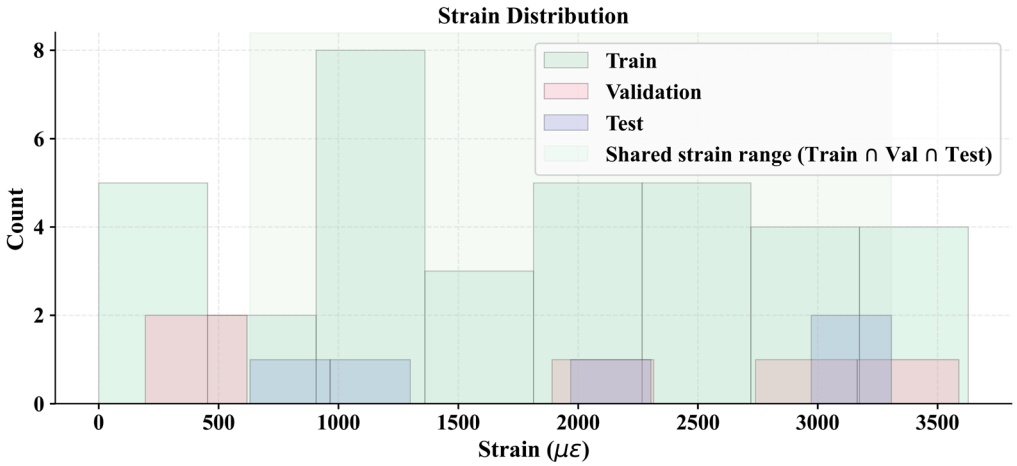


Figure 2. Strain distribution across the training, validation, and test sets.

AWGN augmentation is applied exclusively to the training spectra to improve robustness to measurement perturbations. The original clean spectra are retained, while noise-perturbed versions are added as supplemental training samples. The validation set remains clean during augmentation selection, and the held-out test set remains unchanged, ensuring that neither augmentation tuning nor model selection uses test information.

4.2. SNN Hyperparameters and Implementation

The proposed SNN is implemented as a two-hidden-layer spiking multilayer perceptron with $T = 8$ temporal steps. The hidden layers contain 384 and 160 neurons, respectively, with membrane decay factor $\beta = 0.9$ and firing threshold $V_{th} = 1$. The final spiking representation is decoded through the regression head to estimate the three target peak wavelengths.

The number of temporal steps is treated as an implementation hyperparameter rather than a physical sensing parameter. Candidate values $T = \{2, 4, 6, 8, 10, 12, 14, 16\}$ are evaluated using repeated validation, as shown in Figure 3. The mean validation MSE reaches its minimum at $T = 8$, as indicated by the star in Figure 3, which also satisfies the one-standard-error (SE) selection criterion. Increasing the number of temporal steps beyond $T = 8$ does not improve validation performance and increases computational cost. Therefore, $T = 8$ is selected for the final SNN configuration without reference to the held-out test set.

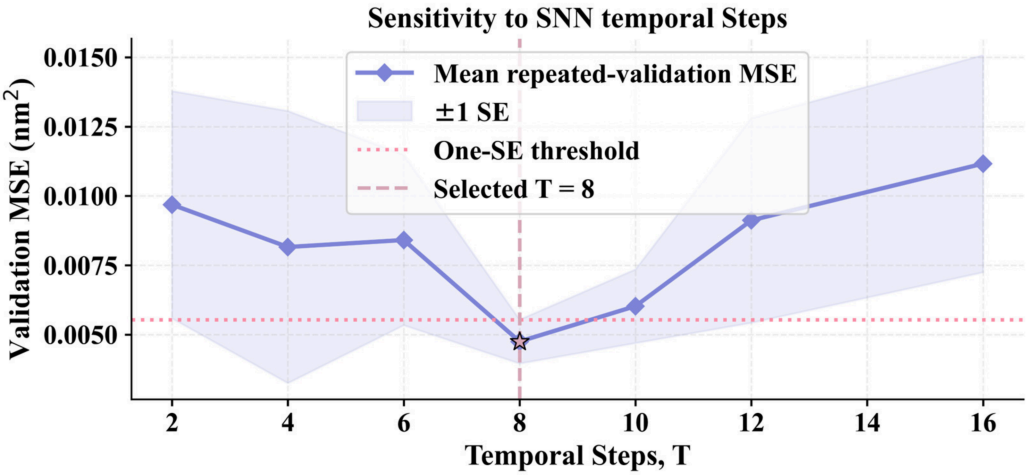


Figure 3. Sensitivity of validation MSE to SNN temporal steps, with mean repeated-validation performance, ±1 SE, and the selected $T = 8$.

To ensure a consistent and fair comparison, the SNN, MDN, LSTM, and GRU follow the same experimental protocol. All models use identical training, validation, and held-out test partitions, the same training-derived normalization, batch size, maximum epoch budget, AWGN augmentation policy, early-stopping criterion, and validation-based model-selection procedure. Hyperparameters are selected using the same validation protocol, while architecture-specific parameters are configured according to the requirements of each model. The principal architectural configurations and training settings of all compared models are summarized in Table 1, including the SNN hidden-layer structure and temporal parameters, the MDN mixture and hidden-layer configuration, and the recurrent-layer settings of the LSTM and GRU. This controlled procedure limits performance differences arising from unequal data handling or model-selection conditions and provides a reproducible basis for comparing demodulation accuracy.

Table 1. Major architectural and training hyperparameters of the compared models.

Parameter	Value
LIF-SNN	Hidden layers: 384, 160 neurons; $T = 8$; $\beta = 0.9$; $V_{th} = 1$
MDN	Hidden layers: 256, 256 neurons; mixture components: 5
LSTM	Hidden size: 32; recurrent layers: 2; dropout: 0.10
GRU	Hidden size: 32; recurrent layers: 2; dropout: 0.10
Learning Rate	0.005
Epochs	220
Optimizer	Lion
Batch size	256
AWGN augmentation ratio	25%
Training SNR range	30–50 dB
Activation function	Gaussian error linear unit (GELU)
Gradient clipping	5

Figure 4 presents the SNN optimizer comparison, where Lion, Adam, AdamW, and stochastic gradient descent (SGD) are evaluated under identical training and validation conditions. Lion achieves the lowest validation MSE and is therefore selected as the optimizer used uniformly for the final SNN, MDN, LSTM, and GRU training. With Lion fixed, Figure 5 evaluates the learning-rate candidates and identifies the operating learning rate adopted for the subsequent model training.

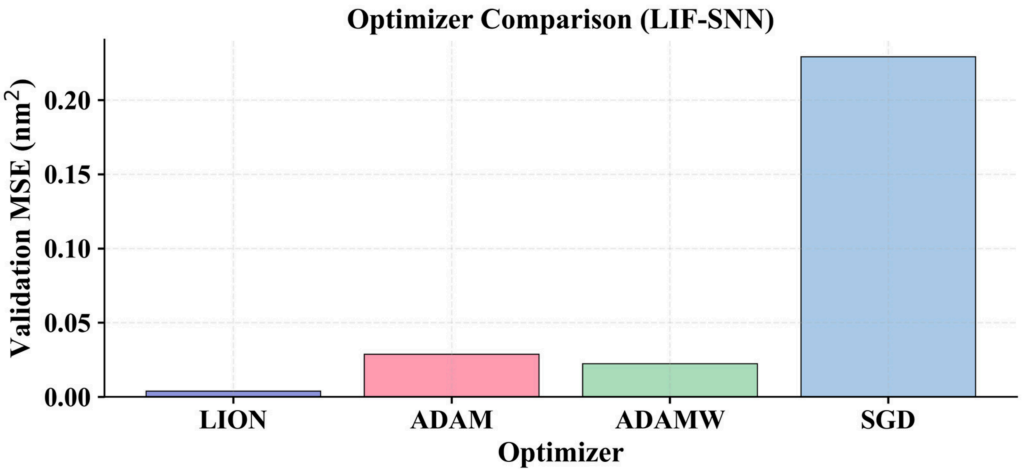


Figure 4. Optimizer comparison for SNN training based on validation MSE.

Using the selected Lion optimizer, the influence of the learning rate is evaluated in Figure 5. Candidate learning rates of 0.0005, 0.001, 0.002, 0.005, and 0.01 are examined using the same validation criterion. A learning rate of 0.005 produces the lowest validation MSE and is therefore adopted for the final model-training configuration.

The influence of the AWGN augmentation ratio is further evaluated using multi-seed experiments, as shown in Figure 6. Augmentation ratios of 0%, 25%, 50%, 75%, and 100% are compared, and the selection is based on the aggregated clean-validation MSE rather than the outcome of a single random initialization. The 25% augmentation ratio provides the lowest validation error and is therefore selected for final training. The injected AWGN spans an SNR range of 30–50 dB, while the validation data remain clean throughout the augmentation-selection procedure. This approach allows the augmentation level to be

selected according to its effect on generalization to unperturbed measurements rather than its performance on artificially corrupted validation data.

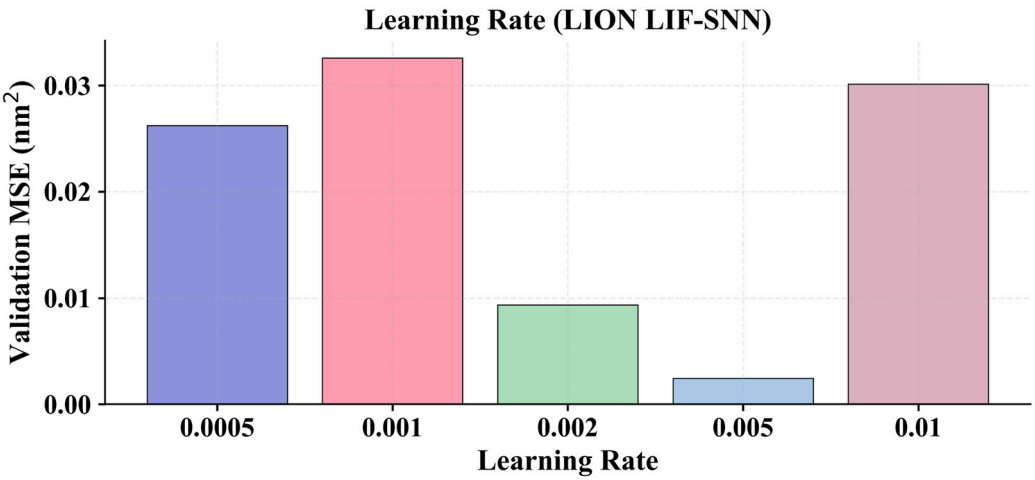


Figure 5. Learning-rate comparison for Lion-based SNN training using validation MSE.

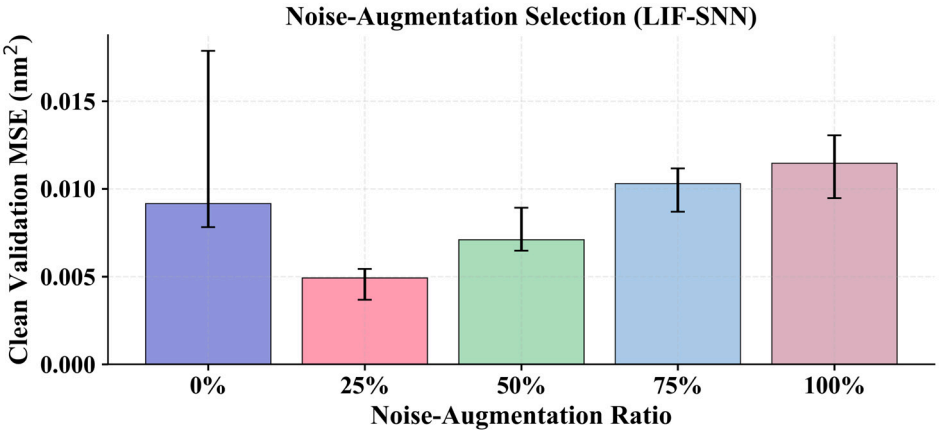


Figure 6. Multi-seed AWGN augmentation-ratio selection based on clean-validation MSE.

The final models are trained for up to 220 epochs with a batch size of 256, with early stopping based on validation loss to limit overfitting. Few-shot adaptation is analyzed over 0–100 gradient-update steps to characterize convergence behavior, while the final operating point is selected using validation performance. The selected configuration uses 9 gradient updates for subsequent evaluation.

The computational experiments are conducted on a 64-bit workstation equipped with an AMD Ryzen 7 8700G processor operating at 4.20 GHz, 16 GB random-access memory (RAM), and an NVIDIA RTX PRO 4000 Blackwell graphics processing unit (GPU) with 24 GB dedicated memory.

5. Results and Discussion

The proposed SNN is evaluated on the held-out test set in terms of few-shot adaptation, wavelength-demodulation error, adaptation computational cost, peak-specific error behavior, and noise robustness. Comparisons with MDN, LSTM, and GRU are performed using the same data partitions and evaluation protocol.

Figure 7 compares the few-shot adaptation behavior of pretrained and scratch-initialized SNNs over successive gradient updates. The pretrained model starts with a substantially lower MSE and maintains a clear advantage throughout adaptation, while the scratch model improves more gradually and remains at a higher error level. This

persistent separation indicates that pretraining provides a more informative initialization for overlap-affected wavelength regression and supports more effective adaptation when only limited target-condition data are available.

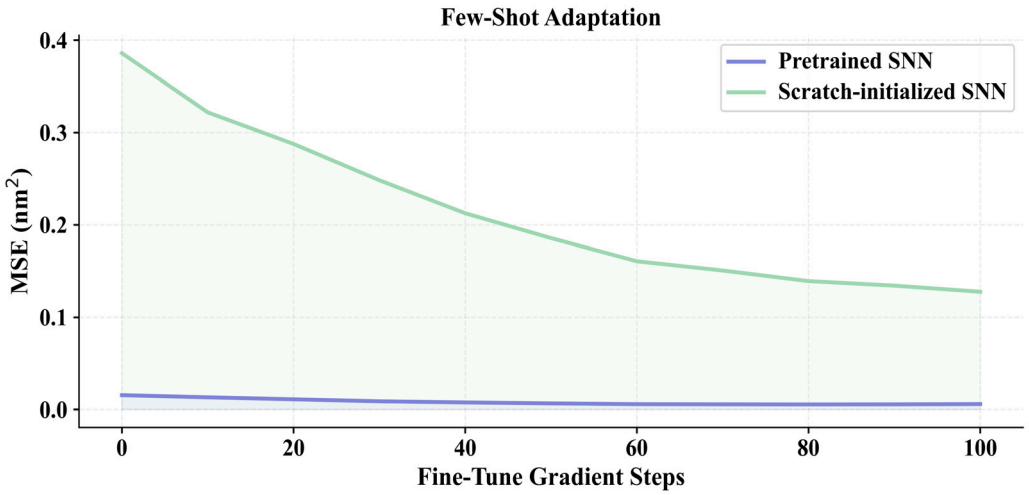


Figure 7. Few-shot adaptation of pretrained and scratch-initialized SNN models.

The practical effect of the adaptation budget is further quantified in Figure 8. The pre-fine-tuning MSE is shown as a constant reference because it represents the prediction error before any adaptation is applied, whereas the post-fine-tuning MSE decreases as the number of gradient updates increases. The reduction is most pronounced during the early adaptation stage and becomes progressively smaller as the update budget increases, indicating diminishing returns at larger numbers of steps. At the same time, the cumulative fine-tuning time increases approximately linearly with the number of updates. The operational adaptation setting is selected independently within the predefined 0–12-step validation search, resulting in 9 gradient updates. At this operating point, the held-out test MSE decreases from 0.0130 nm^2 before adaptation to 0.0085 nm^2 after adaptation, corresponding to a 34.27% reduction. The extended 0–100-step curve is therefore used only to characterize the accuracy–computation tradeoff and is not used to determine the operational fine-tuning configuration.

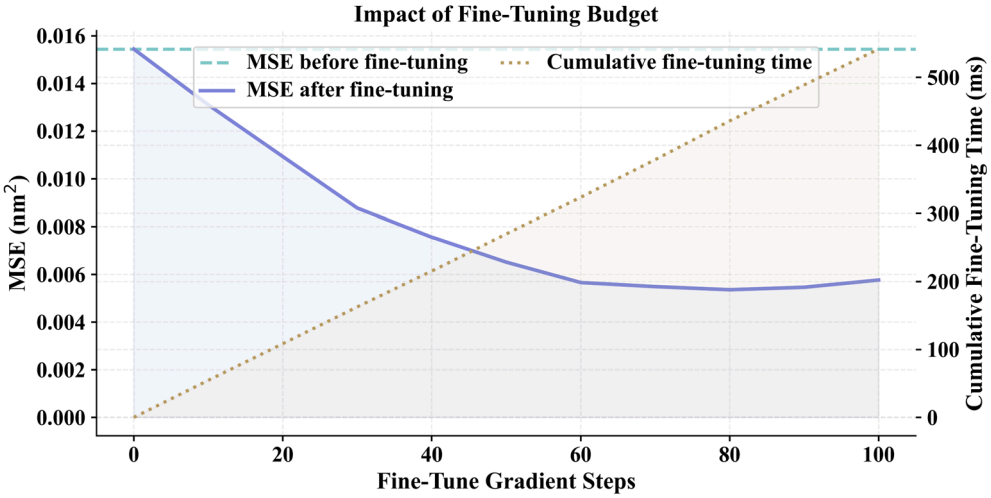


Figure 8. Effect of fine-tuning budget on MSE and cumulative adaptation time.

After establishing the adaptation behavior, the final wavelength-demodulation performance is compared with the MDN, LSTM, and GRU baselines in Figure 9. The proposed

SNN achieves an MAE of 0.0786 nm, an MSE of 0.0130 nm^2, and a mean percentage error (MPE) of 0.0051% on the held-out test set. The MDN produces higher errors, while the LSTM and GRU exhibit substantially larger deviations across the evaluated metrics. In terms of MSE, the SNN reduces the error by approximately 84.7% relative to the MDN and by approximately 97.0% relative to the recurrent baselines. The consistency of these results across independent training runs is further examined in Figure 10.

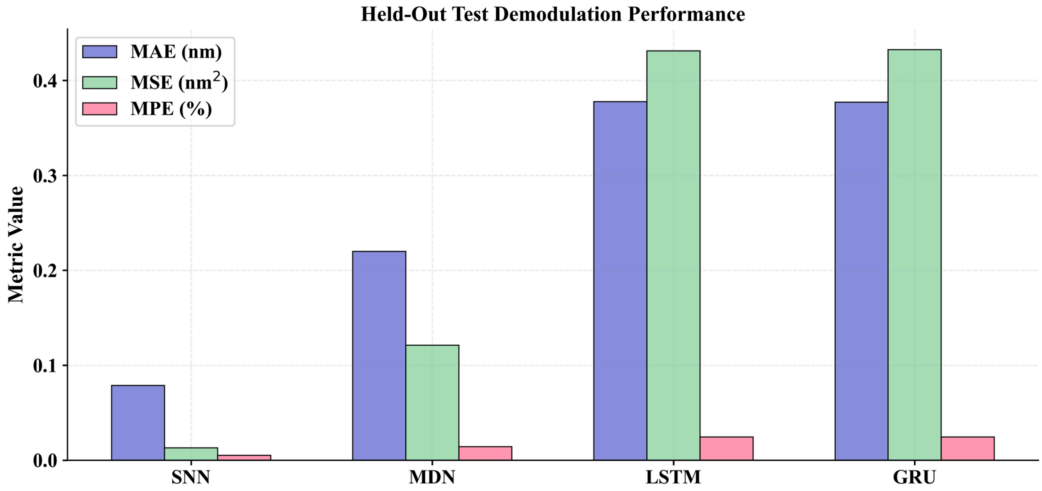


Figure 9. Demodulation performance of the compared models on the held-out test set.

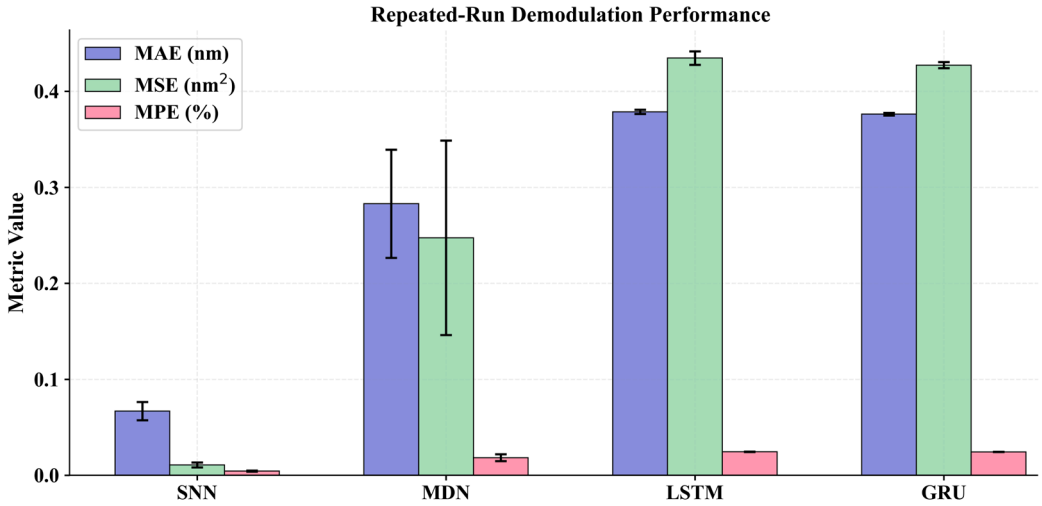


Figure 10. Repeated-run demodulation performance of the compared models, reported as mean MAE, MSE, and MPE with 95% confidence intervals.

Figure 10 further evaluates model stability across repeated training runs using different random seeds, with mean performance reported together with 95% confidence intervals. For MAE, the SNN achieves the lowest mean error of 0.0669 nm, with a 95% confidence interval of 0.0574–0.0764 nm, clearly below those of the MDN, LSTM, and GRU. This separation indicates that the SNN advantage is consistently observed across runs rather than resulting from a single favorable initialization. The MDN shows the largest run-to-run variability, while the LSTM and GRU have narrow confidence intervals but consistently higher errors. These results reinforce the single-run findings in Figure 9 and quantify the uncertainty associated with stochastic training.

The corresponding sample-level error distributions are presented in Figure 11. The SNN exhibits the lowest median absolute error and the most compact distribution among the compared models. In contrast, the MDN shows a wider interquartile range and larger

upper deviations, whereas the LSTM and GRU exhibit substantially broader distributions with extended upper whiskers. The compact SNN distribution indicates that its performance is not driven only by a small number of favorable samples but is maintained more consistently across the held-out spectra. This result is particularly important for wavelength demodulation because occasional large deviations can cause erroneous peak assignment or unstable strain tracking even when the average error remains moderate.

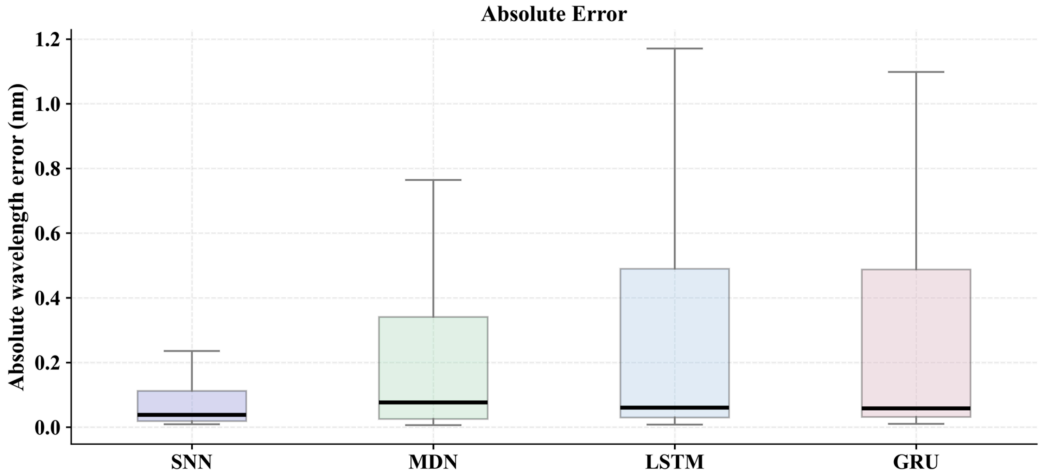


Figure 11. Absolute wavelength-error distributions of the compared models on the held-out test set.

The effect of measurement noise is evaluated explicitly in Figure 12 using AWGN-corrupted derivatives of the held-out clean-test spectra. The SNR values are 30, 35, 40, 45, and 50 dB. Across the investigated SNR range, the proposed SNN maintains the lowest MAE among the evaluated models. Its prediction error decreases as the SNR increases, while the MDN shows substantially stronger degradation under lower-SNR conditions. The LSTM and GRU remain at comparatively high error levels across the tested range. These results provide direct quantitative evidence of the noise robustness of the proposed framework under controlled spectral degradation, rather than relying solely on the theoretical properties of LIF dynamics. The combination of temporal spike integration and validation-selected AWGN augmentation enables the SNN to preserve useful wavelength information under degraded spectral conditions. The observed trend is consistent with recent noise-robust SNN studies, in which spike-based temporal processing combined with noise-aware training or encoding produced smaller performance degradation under corrupted inputs [27].

To separate the effect of the spiking architecture from that of the training strategies, the LIF-SNN is compared with a matched non-spiking MLP under four conditions: without AWGN or few-shot adaptation, with AWGN only, with few-shot adaptation only, and with both AWGN and few-shot adaptation. Comparing the LIF-SNN and MLP under the same training condition indicates the architectural effect, whereas comparing training conditions within the same architecture indicates the effects of AWGN augmentation and few-shot adaptation. Figure 13 shows that the observed performance is not due to the spiking architecture alone. On clean spectra, the matched non-spiking MLP remains competitive with the LIF-SNN, indicating that the feedforward regression structure already provides strong wavelength-estimation capability. Under AWGN-augmented conditions, however, the LIF-SNN shows a clearer advantage, indicating that the spiking dynamics are particularly beneficial when combined with noise-aware training. This trend is consistent with prior studies reporting improved robustness when spiking dynamics are combined with noise-aware training or encoding [27]. Few-shot adaptation provides an additional performance improvement under the evaluated conditions. Therefore, the overall perfor-

mance results from the combined effects of the regression backbone, spiking dynamics, AWGN augmentation, and adaptation.

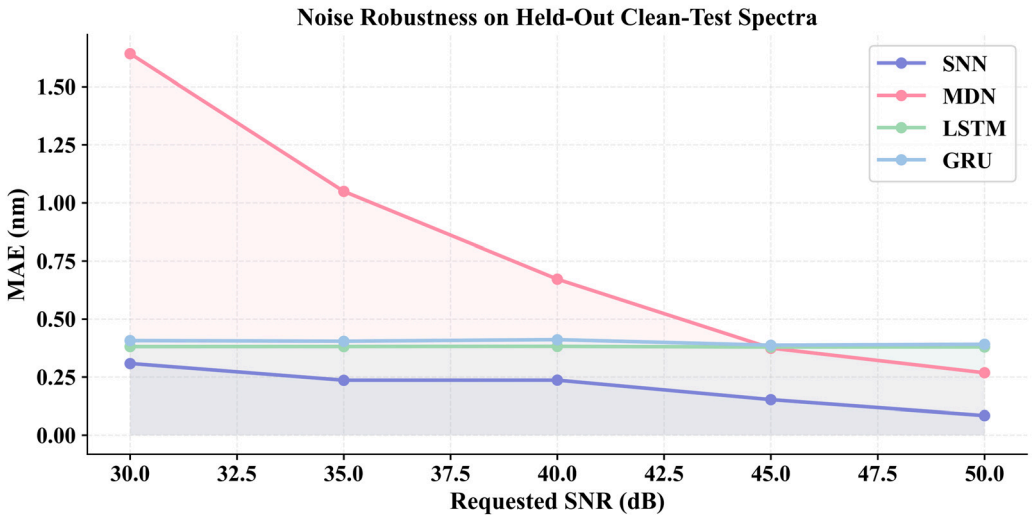


Figure 12. SNR-dependent robustness of the compared models.

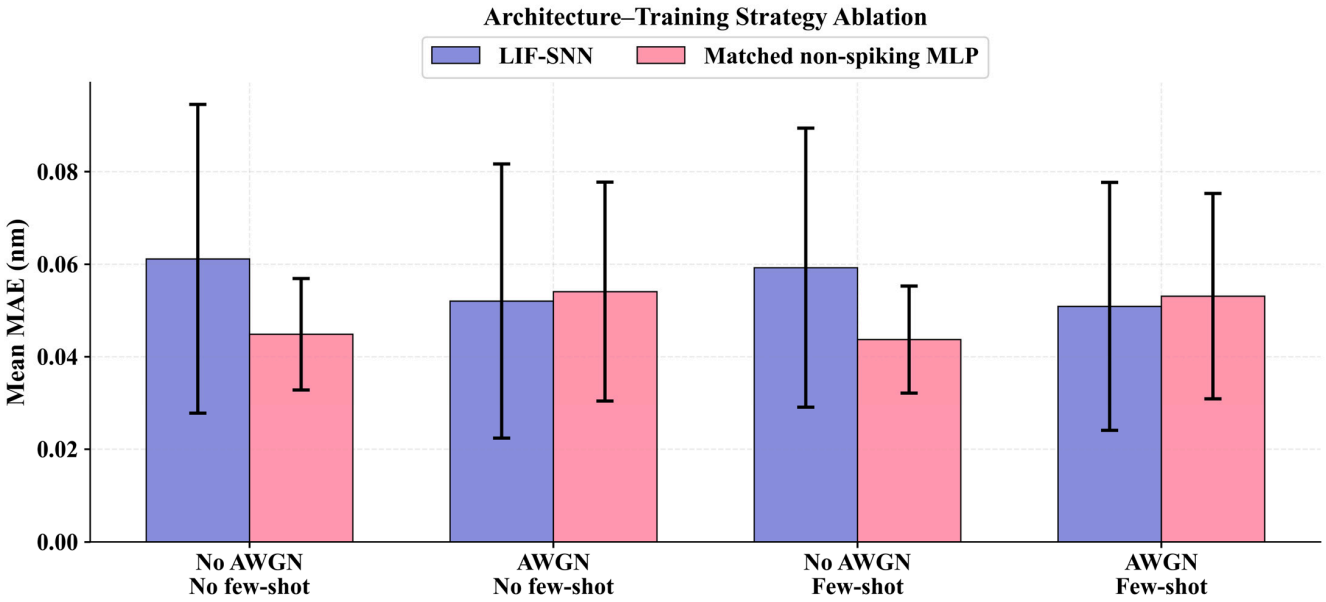


Figure 13. Architecture–training strategy ablation comparing the LIF-SNN and matched non-spiking MLP under AWGN augmentation and few-shot adaptation conditions.

Figure 14 provides a peak-specific assessment of the proposed SNN demodulation performance on the held-out test set. The network directly estimates the three underlying wavelength components from the composite spectrum, namely the strain-dependent FBG Bragg wavelength $\hat{\lambda}_B$, the PMFBG fast-axis wavelength $\hat{\lambda}_f$, and the PMFBG slow-axis wavelength $\hat{\lambda}_s$. The corresponding absolute wavelength errors reveal a clear difference in demodulation difficulty among the three outputs. The FBG component exhibits the largest error spread because its wavelength shifts across the sensing window and experiences varying degrees of spectral overlap with the two PMFBG reflections. In contrast, no mechanical strain is intentionally applied to the PMFBG, so the fast- and slow-axis wavelengths remain approximately stationary. Small variations in these two wavelengths can nevertheless occur during the experiment because of residual room-temperature fluctu-

ations and measurement-related spectral drift, and these effects are treated as part of the experimental background rather than as controlled sensing inputs.

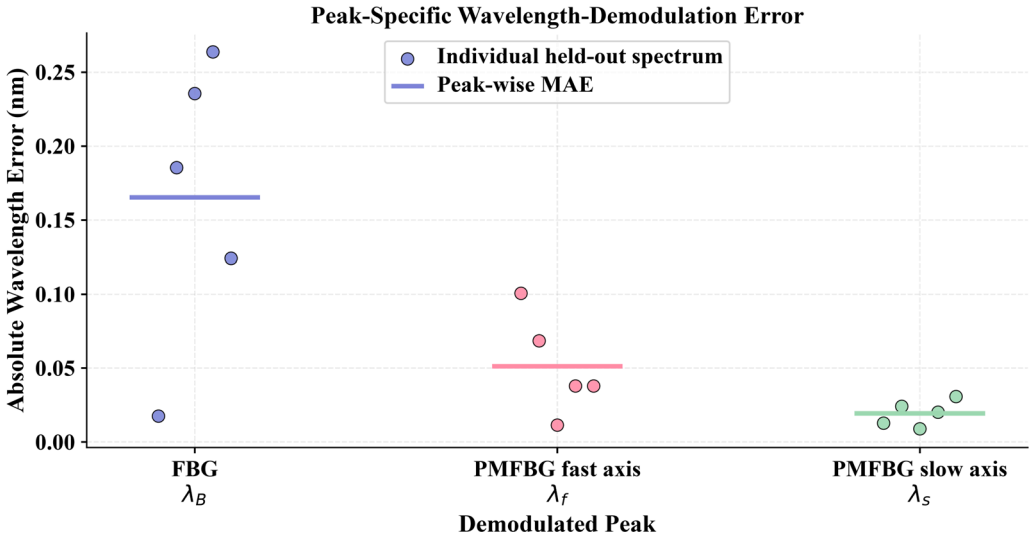


Figure 14. Peak-specific wavelength-demodulation performance.

The peak-wise mean absolute errors are 0.165 nm for $\hat{\lambda}_B$, 0.051 nm for $\hat{\lambda}_f$, and 0.019 nm for $\hat{\lambda}_s$. Although the strain-dependent FBG component exhibits a larger error than the PMFBG fast- and slow-axis outputs, its absolute demodulation error remains low, and the proposed SNN reliably recovers all three wavelength components from the congested composite spectra. The more compact PMFBG errors are consistent with their approximately stationary spectral positions, while their small nonzero deviations reflect residual experimental fluctuations. This peak-specific analysis complements the aggregate metrics by confirming accurate direct three-peak wavelength demodulation without explicit spectral separation and shows that the moving FBG peak is comparatively more challenging because it experiences changing degrees of overlap with the PMFBG reflections.

6. Conclusions

This paper presents an intelligent LIF-SNN framework for direct demodulation of spectrally overlapped FBG–PMFBG responses in fiber-optic strain sensing. The method directly maps each measured composite spectrum to the three underlying peak wavelengths corresponding to the strain-sensitive FBG and the PMFBG fast- and slow-axis responses, avoiding explicit peak separation and conventional peak tracking. Surrogate-gradient learning and temporal spike integration enable end-to-end three-peak regression, while validation-selected AWGN augmentation and few-shot fine-tuning improve robustness and adaptation under limited measured data.

Experiments on held-out measured spectra show that the proposed SNN generalizes to unseen measurements within the experimentally investigated overlap domain and achieves lower wavelength-estimation error than the MDN, LSTM, and GRU baselines under the same evaluation protocol. Peak-wise analysis confirms reliable recovery of all three wavelength components as the moving FBG peak transitions through different overlap severities with the PMFBG reflections. Few-shot adaptation further reduces estimation error, and controlled SNR testing demonstrates comparatively stable performance under noise-degraded spectral conditions.

Overall, the proposed framework provides accurate, adaptive, and noise-robust three-peak demodulation for congested hybrid FBG–PMFBG spectra. The results demonstrate the feasibility of combining direct wavelength regression, limited-data adaptation, and

noise-robust learning within a unified SNN framework, providing a practical basis for future extension to more complex multiplexed and hybrid fiber-sensor systems.

Author Contributions: Conceptualization, B.S., C.-K.Y. and P.-C.P.; methodology, B.S., C.-K.Y., W.-L.W. and Y.-L.C. (Ya-Lin Chen); data preparation, B.S., W.-L.W. and Y.-L.C. (Ya-Lin Chen); model validation, B.S., C.-Z.T. and P.-C.L.; formal analysis, B.S., C.-K.Y., W.-L.W., Y.-L.C. (Ya-Lin Chen), C.-Z.T., P.-C.L., Y.C.M., A.M.D., Y.-L.C. (Yang-Lang Chang) and P.-C.P.; investigation, B.S., C.-K.Y., W.-L.W., Y.-L.C. (Ya-Lin Chen), C.-Z.T., P.-C.L., Y.C.M., A.M.D., Y.-L.C. (Yang-Lang Chang) and P.-C.P.; writing—original draft preparation, B.S.; writing—review and editing, B.S., C.-K.Y., Y.C.M. and A.M.D.; supervision, Y.-L.C. (Yang-Lang Chang) and P.-C.P. All authors have read and agreed to the published version of the manuscript.

Funding: This work was supported by the National Science and Technology Council, Taiwan, under Grant NSTC 115-2221-E-027-060-MY2.

Institutional Review Board Statement: Not applicable.

Informed Consent Statement: Not applicable.

Data Availability Statement: The data presented in this study are available in this article.

Conflicts of Interest: The authors declare no conflicts of interest.

References

1. López-Higuera, J.M.; Rodriguez Cobo, L.; Quintela Incera, A.; Cobo, A. Fiber optic sensors in structural health monitoring. *J. Light. Technol.* **2011**, *29*, 587–608. [CrossRef]
2. Golovastikov, N.V.; Kazanskiy, N.L.; Khonina, S.N. Optical fiber-based structural health monitoring: Advancements, applications, and integration with artificial intelligence for civil and urban infrastructure. *Photonics* **2025**, *12*, 615. [CrossRef]
3. Poulopoulos, G.; Avramopoulos, H. Review of optical fiber and integrated photonic sensors for industry and smart manufacturing: Technologies, applications, structural health monitoring and AI-enabled sensing. *Sensors* **2026**, *26*, 3581. [CrossRef] [PubMed]
4. Hui, R.; O'Sullivan, M. *Fiber-Optic Measurement Techniques*, 2nd ed.; Academic Press: Cambridge, MA, USA, 2022.
5. Zhang, H.; Zhai, X.; Sun, J. Application prospects of optical fiber sensing technology in smart campus construction: A review. *Photonics* **2025**, *12*, 1026. [CrossRef]
6. Her, S.C.; Lin, W.N. Simultaneous measurement of temperature and mechanical strain using a fiber Bragg grating sensor. *Sensors* **2020**, *20*, 4223. [CrossRef] [PubMed]
7. Yang, S.H.; Yao, C.K.; Dehnaw, A.M.; Zhuang, Y.Q.; Peng, P.C. A dual-FBG sensor with machine learning for microstrain–temperature decoupling under cyanoacrylate bonding toward catheter applications. *Micromachines* **2026**, *17*, 682. [CrossRef] [PubMed]
8. Ning, X.; Murayama, H.; Kageyama, K.; Wada, D.; Kanai, M.; Ohsawa, I.; Igawa, H. Dynamic strain distribution measurement and crack detection of an adhesive-bonded single-lap joint under cyclic loading using embedded FBG. *Smart Mater. Struct.* **2014**, *23*, 105011. [CrossRef]
9. Xu, X.; Wang, Y.; Zhu, D.; Shi, J. Accurate strain extraction via kernel extreme learning machine for fiber Bragg grating sensor. *IEEE Sens. J.* **2022**, *22*, 7792–7797. [CrossRef]
10. Cao, Z.; Zhang, S.; Xia, T.; Liu, Z.; Li, Z. Spectral demodulation of fiber Bragg grating sensor based on deep convolutional neural networks. *J. Light. Technol.* **2022**, *40*, 4429–4435. [CrossRef]
11. Manie, Y.C.; Peng, P.C.; Shiu, R.K.; Hsu, Y.T.; Chen, Y.Y.; Shao, G.M.; Chiu, J. Enhancement of the multiplexing capacity and measurement accuracy of FBG sensor system using IWDM technique and deep learning algorithm. *J. Light. Technol.* **2020**, *38*, 1589–1603. [CrossRef]
12. Rudloff, G.; Soto, M.A. Multipeak wavelength detection of spectrally overlapped fiber Bragg grating sensors through a CNN-based autoencoder. *IEEE Sens. J.* **2024**, *24*, 20674–20687. [CrossRef]
13. Sarkar, S.; Inupakutika, D.; Banerjee, M.; Tarhani, M.; Shadaram, M. Machine learning methods for discriminating strain and temperature effects on FBG-based sensors. *IEEE Photon. Technol. Lett.* **2021**, *33*, 876–879. [CrossRef]
14. Xu, H.; Chen, S.; Ren, S.; Hou, X.; Peng, H.; Wang, G.; Zhang, Y. High-resolution spectrum reconstruction of cascaded FBG-FPI sensor in resource-constrained environments. *IEEE Sens. J.* **2024**, *24*, 11878–11885. [CrossRef]
15. Liu, P.; Xu, Z.; Wang, Y.; Jiang, L.; Wu, M. Optimized demodulation of highly overlapped fiber Bragg grating sensor networks using two-stage deep learning approach. *Opt. Eng.* **2024**, *63*, 046103. [CrossRef]

16. Yao, C.K.; Lin, H.P.; Cheng, C.L.; Li, Y.L.; Du, L.Y.; Peng, P.C. Satellite communication and free space optics for open radio access network. *J. Light. Technol.* **2024**, *42*, 3546–3553. [CrossRef]
17. Dehnaw, A.M.; Chang, C.Y.; Yao, C.K.; Ho, M.J.; Hu, N.T.; Chen, C.S.; Peng, P.C. FBG sensor-integrated robotic arm motion and joint-angle recognition using heterogeneous ensemble stacked generalization learning. *IEEE Sens. J.* **2026**, *26*, 31114–31124. [CrossRef]
18. Shen, G.; Zhao, D.; Zeng, Y. Exploiting high performance spiking neural networks with efficient spiking patterns. *IEEE Trans. Emerg. Top. Comput. Intell.* **2025**, *9*, 1480–1489. [CrossRef]
19. Shooshtari, M.; Serrano-Gotarredona, T.; Linares-Barranco, B. Review of memristors for in-memory computing and spiking neural networks. *Adv. Intell. Syst.* **2026**, *8*, e202500806. [CrossRef]
20. Zhang, A.; Li, X.; Gao, Y.; Niu, Y. Event-driven intrinsic plasticity for spiking convolutional neural networks. *IEEE Trans. Neural Netw. Learn. Syst.* **2022**, *33*, 1986–1995. [CrossRef] [PubMed]
21. Zhu, M.; Murayama, H.; Wada, D.; Kageyama, K. Dependence of measurement accuracy on the birefringence of PANDA fiber Bragg gratings in distributed simultaneous strain and temperature sensing. *Opt. Express* **2017**, *25*, 4000–4017. [CrossRef] [PubMed]
22. Zhao, Y.; Sun, B.; Liu, Y.; Ren, J.; Zhang, J.; Yang, J.; Canning, J.; Peng, G.D.; Yuan, L. Polarization mode coupling and related effects in fiber Bragg grating inscribed in polarization-maintaining fiber. *Opt. Express* **2016**, *24*, 611–619. [CrossRef] [PubMed]
23. Jiang, Z.; Yin, B.; Sang, G.; Zhang, Y.; Zhao, Y.; Pei, L.; Wu, S.; Yu, F. Three-wavelength laser sensor for2-D vector magnetic field measurement with temperature self-compensation. *IEEE Trans. Instrum. Meas.* **2026**, *75*, 9529813. [CrossRef]
24. Wu, Y.; Deng, L.; Li, G.; Zhu, J.; Shi, L. Spatio-temporal backpropagation for training high-performance spiking neural networks. *Front. Neurosci.* **2018**, *12*, 331. [CrossRef] [PubMed]
25. Yan, Z.; Tang, K.; Zhou, J.; Wong, W.-F. Low latency conversion of artificial neural network models to rate-encoded spiking neural networks. *IEEE Trans. Neural Netw. Learn. Syst.* **2025**, *36*, 14107–14118. [CrossRef] [PubMed]
26. Dampfhoffer, M.; Mesquida, T.; Valentian, A.; Anghel, L. Backpropagation-based learning techniques for deep spiking neural networks: A survey. *IEEE Trans. Neural Netw. Learn. Syst.* **2024**, *35*, 11906–11921. [CrossRef] [PubMed]
27. Yang, J.; Kim, S. Noise robust SAR image classification using Siamese spiking neural networks. *IEEE Geosci. Remote Sens. Lett.* **2024**, *21*, 4017205. [CrossRef]

Disclaimer/Publisher's Note: The statements, opinions and data contained in all publications are solely those of the individual author(s) and contributor(s) and not of MDPI and/or the editor(s). MDPI and/or the editor(s) disclaim responsibility for any injury to people or property resulting from any ideas, methods, instructions or products referred to in the content.